Comparison of a Liquid Crystal Point-Diffraction Interferometer and a Commercial Phase-Shifting Interferometer

Introduction

Fusion-class lasers, such as OMEGA, typically require hundreds, or even thousands, of high-performance optical elements ranging in diameter from several millimeters to tens of centimeters. To obtain high irradiation uniformity required for direct-drive ICF, it is critical that (1) the optical performance of these elements and associated optical subsystems be well characterized before being installed in the laser, and (2) their high performance be maintained throughout their lifetime in the laser system. Commercially available Fizeau phase-shifting interferometers[1] with aperture sizes of between 4 and 18 in. have been used to characterize the laser beam wavefront before optical elements are installed on OMEGA. Although these interferometers have high sensitivity, their expense and susceptibility of the measurement to environmental disturbance scale significantly with aperture size. Once optical elements are installed into OMEGA, wavefront characterization of OMEGA beamlines is performed at $\lambda = 1054$ nm with a shearing interferometer,[2] but the method suffers from (1) an inability to perform gradient measurements in more than two directions, (2) a sensitivity to only low-order phase errors, and (3) low spatial resolution. We have investigated the use of a phase-shifting, point-diffraction interferometer (PDI) both as a replacement to the shearing interferometer and as a low-cost alternative to commercially available phase-shifting interferometers.

The PDI[3,4] is an elegantly simple device that consists of a pinhole, upon which a laser beam under test is focused, and a region of high optical density surrounding the pinhole, which is used to attenuate a portion of the incident beam. Light diffracted from the pinhole generates a reference wavefront, while light that propagates around the pinhole is the object beam under test. Interference fringes of high contrast are obtained by attenuating the object beam such that object and reference beam intensities are nearly equal. A distinct advantage of the PDI design is its truly common-path nature, i.e., both object and reference beams follow the same path as opposed to two different paths, such as in the Mach–Zehnder, Michelson, or Fizeau interferometers.[5] This attribute makes the PDI an attractive alternative to other interferometers for several reasons: (1) sensitivity to environmental disturbances such as mechanical vibration, temperature fluctuations, and air turbulence is reduced; (2) very short coherence length lasers can be used, without the need for path-length-adjusting optics to maintain high fringe visibility; and (3) fewer optical elements are required, reducing the size and cost of the instrument. Several modifications of the PDI to incorporate the phase-shifting technique are described in the literature;[6] however, the liquid crystal point-diffraction interferometer (LCPDI), introduced by Mercer and Creath,[7,8] is particularly attractive because of its simplicity, ease of use, and low manufacturing cost. The LCPDI maintains the advantages of the standard PDI, while providing an ability to phase-shift the object beam wavefront relative to the reference wavefront. It is a modification of the PDI, where the pinhole that generates the reference wavefront is replaced by a glass or plastic microsphere that is embedded within a nematic liquid crystalline "host" (see Fig. 83.29). A voltage applied to the liquid crystal (LC) cell

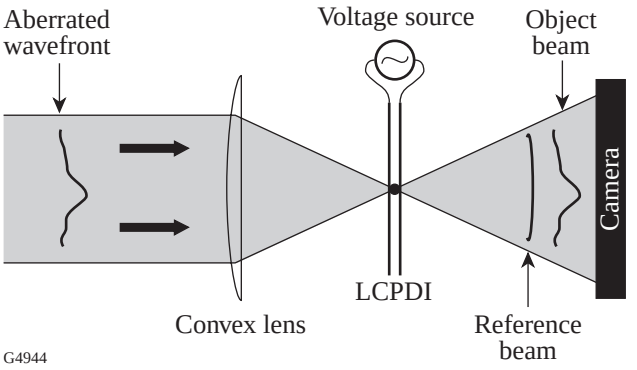

Figure 83.29
Schematic diagram of the liquid crystal point-diffraction interferometer (LCPDI). The laser beam is focused onto an area of the device containing a glass or plastic microsphere in the LC fluid gap that takes the place of the pinhole in the standard point-diffraction interferometer (PDI). The portion of the beam passing through the microsphere forms the reference wavefront of the interferometer, and light passing around the microsphere forms the object beam under test. Phase-shifting is accomplished through the application of an electric field to the LCPDI, as described in Fig. 83.30.

causes a phase shift of the object beam relative to the diffracted reference beam by an effective refractive index change of the LC. A "guest" dye that is added to the liquid crystalline host improves fringe contrast by attenuating the object beam intensity. Notably, the phase-shifting LCPDI was shown by Mercer and Rashidnia to be significantly more robust when compared with a phase-shifting Mach–Zehnder interferometer.[9]

We compared a visible-wavelength LCPDI to a commercially available, Mark IV XP Fizeau phase-shifting interferometer[10] and found that LCPDI measurements of a witness sample were in close agreement with measurements of the same sample made using the commercially available interferometer. Two systematic, phase-shift error sources in the LCPDI that contributed to measurement discrepancies were (1) an intensity modulation from frame to frame caused by the dichroism of the dye[8] and, to a lesser extent, (2) molecular alignment distortions of the host liquid crystal around the microsphere.[11] These phase-shift errors currently produce a spatially dependent accuracy in the LCPDI that, in some regions, closely compares with the Mark IV, but departs from the Mark IV measurements by approximately 50 nm in regions of highest systematic error. A smaller departure of the measurement from that of the Mark IV at higher spatial frequencies was due to interference effects caused by residual reflections between the CCD array and the final imaging lens. By modifying LCPDI fabrication parameters and through judicious choice of phase acquisition and analysis methods, these systematic errors can be significantly reduced.

LCPDI Construction

LCPDI cells were fabricated with liquid crystal Merck E7, a eutectic composition of rodlike molecules that has a nematic phase at room temperature. The long axes of the molecules in the nematic phase have a preferred orientation characterized by a unit vector called the *director*. A thin film of nylon or polyimide was applied to the inner surfaces of indium-tin oxide (ITO)–coated glass substrates and subsequently buffed unidirectionally, causing the director to preferentially lie in the plane of the substrates. Long-range orientational order, which is homogeneous and coincides with the direction of the crystal optic axis, is thereby imparted to the molecules. The means by which the LCPDI phase shifts is shown conceptually in Fig. 83.30. For a homogeneously aligned nematic LC with molecular axis parallel to the cell walls, linearly polarized light along the long axis of the molecule in Fig. 83.30 will see extraordinary refractive index n_e. As voltage is applied to the cell, the LC molecules will reorient, as shown. The effective refractive index approaches the value of the ordinary refractive index n_o when the molecules in the bulk of the fluid are nearly perpendicular to the cell walls. Cell parameters that determine the maximum phase shift are primarily the LC birefringence and fluid path length, assuming that the microsphere diameter and fluid path length are equal. If the microsphere diameter is less than the path length of the cell, phase modulation will be less. In addition, strong anchoring of interfacial LC molecules to the cell walls prevents complete reorientation of the director throughout the fluid path length, resulting in an effective refractive index that is somewhat less than n_o.

Fluid path lengths and microsphere diameters of either 10 or 20 μm were used, and cell gap was maintained by placement of fiber spacers or glass microspheres at the outer edges of the cell. The use of fiber spacers instead of glass microspheres at the corners of the device improved cell gap uniformity and reduced wedge across the clear aperture of the LCPDI device. Glass substrates, 2.4 cm × 2.8 cm × 1 mm thick, had inner walls that were coated with electrically conductive ITO prior to application of the alignment layer. We determined that in this application polyimide alignment layers offer an advantage over nylon layers because (1) they are more resistant to scratches that can be produced while manipulating the microspheres during assembly, and (2) they are easier to spin-deposit and buff, yielding devices with higher alignment

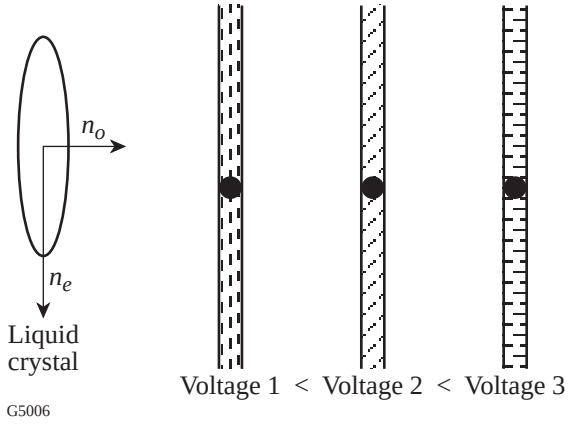

Figure 83.30
An electric field applied to the LCPDI produces a controlled reorientation of the birefringent LC molecules, thereby shifting the phase of the object wavefront relative to the reference wavefront. Light that is polarized along the buff direction of the cell will first see extraordinary refractive index n_e, followed by refractive index values approaching the ordinary refractive index n_o as voltage is applied. Attenuation of the object beam intensity by adding a "guest" dye to the LC fluid "host" allows high-contrast fringes to be obtained.

quality and contrast. Antiparallel buffing on opposing substrate surfaces generally provided better alignment quality than parallel-buffed surfaces. Bonding the wire leads to the devices with conductive epoxy *before* rather than after filling with LC eliminated the infiltration of air into the devices caused by the expansion and contraction of the fluid-filled cell during the epoxy thermal cure process. Visible-wavelength absorbing dye, Oil Red O, at 1% wt/wt concentration, was used for the device designed to operate at $\lambda = 543$ nm and produced an optical density of 2.1 in a 10-μm-path-length cell with no voltage applied. The blocking extinction, or optical density (OD), of this cell at $\lambda = 543$ nm with light polarized along the buffing direction as a function of applied voltage is shown in Fig. 83.31. Because of the absorption dichroism of the dye, the OD of the cell varied between 2.1 and 0.8 as voltage was raised from 0 to 6 V (rms) using a 2-kHz sine wave.

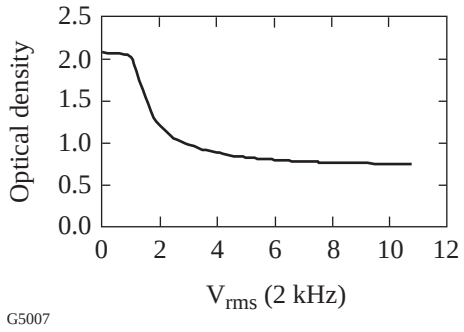

Figure 83.31
Absorbance at $\lambda = 543$ nm of the LCPDI with 1% wt/wt concentration of Oil Red O dye in the nematic E7 host LC as a funtion of voltage applied to the device. The dichroism of the dye produces voltage-dependent changes in fringe intensity and contrast.

Microspheres were placed in the cell using one of two different techniques: In the first method, a large quantity of microspheres were spin deposited onto one of the substrate surfaces before the cell was assembled. This ensured that a microsphere could later be found that would phase modulate satisfactorily upon optical testing and was quite easy to do compared with the manual deposition technique described below. A disadvantage of this approach is the possibility of microsphere agglomeration resulting in optical interference from adjacent microspheres during device testing. The current device assembly protocol calls for a single microsphere to be placed manually in the center of the substrate using a high-power microscope. In this method, the sphere is positioned using a single fiber from a camel's-hair brush. Custom assembly tooling helps to keep the two substrates in registration with each other as they are lowered to help eliminate the scratching of the alignment coating caused by microsphere displacement when the substrates are inadvertently sheared. We have found that the use of glass microspheres rather than plastic ones as the central element reduces the number of scratches in the alignment coating caused by movement of the central sphere during device assembly operations. Plastic spheres also had a slightly elliptical appearance in some cells and showed a uniaxial conoscopic figure, likely due to stress-induced birefringence imparted by the substrates during cell fabrication and epoxy cure. The custom tooling used to maintain substrate registration remedied this by preventing excessive force from being applied during the assembly operation.

Test Sample Measurements

The LCPDI cell used for these measurements had a glass microsphere diameter and fluid gap of 10 μm and was placed in the experimental setup shown in Fig. 83.32. The $\lambda = 543$-nm HeNe laser beam was spatially filtered and up-collimated to slightly overfill a 1-in.-diam *f*/16 doublet lens used to focus the beam into the LCPDI. A Tamron SP60 300-mm telephoto zoom lens was used to image the cavity region to the CCD camera. The beam diameter at the focus of the doublet was 41 μm at $1/e^2$ of peak intensity, as measured with a scanning slit. The intensity onto the LCPDI was adjusted, and linear polarization was maintained along the extraordinary axis of the LC by using two polarizers placed before the spatial filter. Fringe data were acquired through a sequence of five images, each shifted incrementally in phase by a relative amount $\pi/2$, and resultant phase ϕ computed using the five-frame algorithm[8,12,13]

$$\tan(\phi) = \left(\frac{\Delta I_3 - \Delta I_1}{\Delta I_0 + \Delta I_4 - 2\Delta I_2} \right) \times \left(\frac{\sqrt{I_0^{\text{obj}}} + \sqrt{I_4^{\text{obj}}} + 2\sqrt{I_2^{\text{obj}}}}{\sqrt{I_3^{\text{obj}}} + \sqrt{I_1^{\text{obj}}}} \right), \quad (1)$$

where I_k^{obj} is the kth object beam intensity distribution and $\Delta I_k = I_k - I_k^{\text{obj}}$ is the kth interferogram in the five-frame sequence. Equation (1) is normalized to the intensity distribution of the object beam in order to reduce the effect of intensity and contrast changes caused by the dichroism of the dye, as described by Mercer.[8] The object beam intensity was obtained by moving the LCPDI a short distance laterally so that the incident beam did not intersect the microsphere and by acquiring five frames of data at the same voltages used for acquiring interferometric phase data. Table 83.II gives a relative com-

parison of several different phase unwrapping algorithms that were tested with intentionally noisy data (i.e., low-contrast fringes with focus at the microsphere) in order to compare the robustness of the various unwrapping algorithms. In Table 83.II, the relative processing speed of these algorithms is compared to a simple path-dependent, linear algorithm that began at the edge of the CCD array and propagated unacceptably large unwrapping errors throughout the array. The large residual errors for the algorithms listed in the table are primarily from unwrapping errors at the edge of the CCD array. Although a tiled, path-dependent unwrapping algorithm that began in the center of the array, combined with a masking technique, produced the least phase error, the tiled algorithm was chosen without masking because it required significantly less processing time and had only marginally greater residual error. Data acquisition was automated using a personal computer, in-house data acquisition and analysis software, and graphical user interface. With no test sample in the cavity region between the collimating lens and the focusing doublet, several focus and voltage conditions were investigated, as described in Table 83.III. The least amount of residual phase error in empty cavity measurements was found in the low-voltage regime (<1.2-V rms at 2 kHz) with 3 to 4 fringes on the camera. Greater phase error was observed in the high-voltage regime (3.8 to 7 V) because of the loss of fringe contrast caused by the absorption dichroism of the dye.

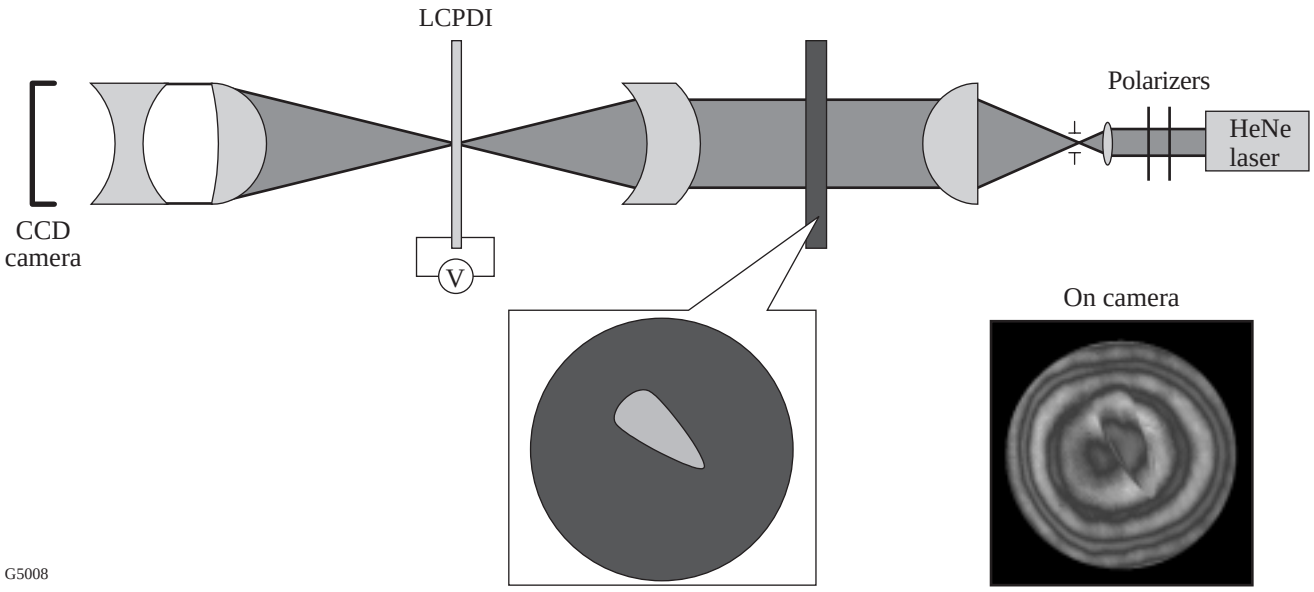

Figure 83.32
Experimental setup used for LCPDI measurements. The inset shows interference fringes from the test sample with an MRF-polished spot.

Table 83.II: Relative comparison of different unwrapping algorithms with intentionally noisy data (low-contrast fringes). Among the algorithms tested, the tile unwrapping algorithms showed the least number of unwrapping errors. The tile unwrapping algorithm with a tile size of 10×10 pixels was used for the experimental results reported.

	Centered Linear, Path Dependent	Box Mask and Linear, Path Independent	Tile Unwrap	Tile Unwrap and Box Mask
p–v (2π rad)	9.07	3.23	2.77	2.670
rms (2π rad)	0.45	0.13	0.10	0.094
Computation time (compared to standard unwrap starting at edge of array)	1:1	3:1	5:2	4:1

To characterize the empty cavity, two sets of ten phase measurements were taken approximately 5 min apart, the ten measurements averaged, and the two sets of phase averages subtracted to give residual peak-to-valley (p–v) and rms phase errors of 22 nm and 1.7 nm, respectively, as shown in Fig. 83.33. The quality of the interference fringes used for the five-frame sequence is shown in Fig. 83.33(a). As evident from the horizontal lineout in Fig. 83.33(b), a residual amount of tilt is present in the phase difference. With tilt removed, p–v and rms phase errors drop to 19 nm and 1.1 nm, respectively. The dominant phase error in Fig. 83.33(b) has a spatial period equal to that of the interference fringes, suggesting that the effect of the dye has not been entirely eliminated through the use of Eq. (1). Also apparent in the phase image is an error term equal to twice the frequency of the fringes, indicating that there is some amount of phase-shift error related to the host LC in addition to the dye-induced error. Because these systematic error sources are present, their removal through subtraction of a reference phase requires stringent control of environmental parameters. Although air turbulence was reduced by placing a plastic enclosure around the setup in Fig. 83.32, the setup was not supported by an air-isolation table and was located in a

Table 83.III: Several focus and voltage conditions were investigated for the LCPDI in empty-cavity measurements.

Focus	– Close to best focus (1 to 2 fringes) – Intermediate focus position (3 to 4 fringes) – Far from best focus (8 to 9 fringes) - Off center (lateral movement of the LCPDI) - On center (no lateral movement)
Voltage (rms at 2 kHz)	– Low-voltage regime (0–1.21 V) – High-voltage regime (3.8–7 V)

Conditions giving least residual phase error: intermediate focus with low-voltage regime.

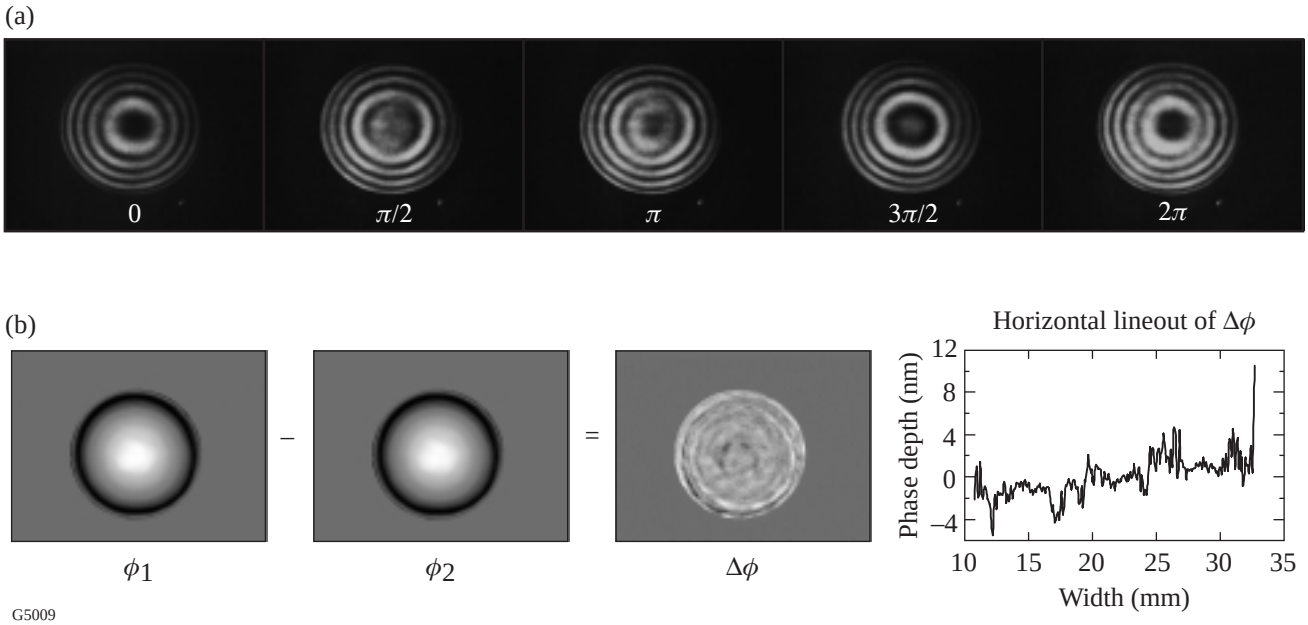

Figure 83.33
(a) LCPDI interference fringes obtained by phase-shifting through 2π rad, from 0.98 V (0) to 1.21 V (2π). (b) Two empty-cavity phase images ϕ_1 and ϕ_2 were subtracted to obtain the residual phase error $\Delta\phi$ in the LCPDI. The phase-difference image reveals phase-error contribution from both dye- and host-induced phase-shift error.

room without strict air-handling requirements. It is expected that more rigorous environmental standards and improvements to LCPDI packaging and mounting will significantly improve its precision. Further improvements to both accuracy and precision of the LCPDI can be achieved through removal or mitigation of systematic error sources, as discussed below.

A test object was next inserted into the cavity that consisted of a 2-in.-diam × 0.25-in.-thick fused-silica wedged window with a central "spot" polished into the window using the magnetorheological finishing method (MRF).[14] The geometry of the polished spot is characteristic of this technique and was well suited for this test because of the co-existence of steep and gradual gradient features (see Fig. 83.32). An empty-cavity phase measurement was subtracted from the phase measurement of the test object for all measurements reported here. In contrast to the empty-cavity measurements described previously, however, acquisition of both the test object phase and associated reference phase incorporated a $\pi/2$ phase-offset technique[12] that reduced residual phase-shift errors at twice the fringe frequency that were apparent in initial measurements of the test piece. In this method, ten phase measurements were acquired per Eq. (1) and averaged, followed by an additional set of ten phase measurements acquired with the first frame of the five-frame sequence offset in phase by $\pi/2$. Averaging the first set of ten measurements with the set of measurements acquired with $\pi/2$ offset produced the phase plot shown in Fig. 83.34. This figure shows that the LCPDI results are in close agreement with those from a 4-in.-aperture Zygo Mark IV XP operating at $\lambda = 633$ nm and located on an air-supported table in the Center for Optics Manufacturing (COM). The close comparison of the high gradient features on the left of the lineout is especially notable. The large peak on the right of the LCPDI lineout appears to approach a discrepancy of 100 nm, but it is near the edge of the aperture, where a valid comparison cannot be made because of the absence of Mark IV XP data. The remaining discrepancies on the right of the lineout are attributed to the following sources: (1) Phase-shift errors likely related to the dichroism of the dye produced an approximately 50-nm residual phase error at the same spatial frequency as the fringe pattern, which can be seen in the LCPDI phase image in Fig. 83.34. (2) The high-spatial-frequency ripple in the LCPDI lineout of Fig. 83.34 was caused by an interference pattern observed during data acquisition whose origin appeared to be multiple reflections between the zoom lens and the CCD array. (3) To a lesser extent, alignment distortions of the host LC molecules may also contribute residual phase-shift error, as discussed below. As noted previously, accounting for object beam intensity changes through the use of Eq. (1) has not completely removed the phase error related to the absorption dichroism of the dye. The phase-offset method, however, reduced the appearance of LC host-induced phase-shift errors at twice the fringe frequency, although higher-order phase-shift error not compensated using this technique may still be present.[15] Because the dominant error has periodicity equal to the interference fringes, the current LCPDI device incorporating the highly dichroic Oil Red O dye would be most useful for characterizing aberrations whose Zernike fit is not significantly affected by the presence of this error.

Discussion

1. Dye-Induced Measurement Error

The predominant phase error in Fig. 83.34 has a periodicity equal to that of the interference fringes, indicating that its most likely origin is an intensity change between phase shifts caused by absorption dichroism of the Oil Red O dye.[8] The use of Eq. (1) significantly reduces the contribution of this effect to the phase error but does not eliminate it entirely. Equation (1) is exact provided that (1) the reference beam

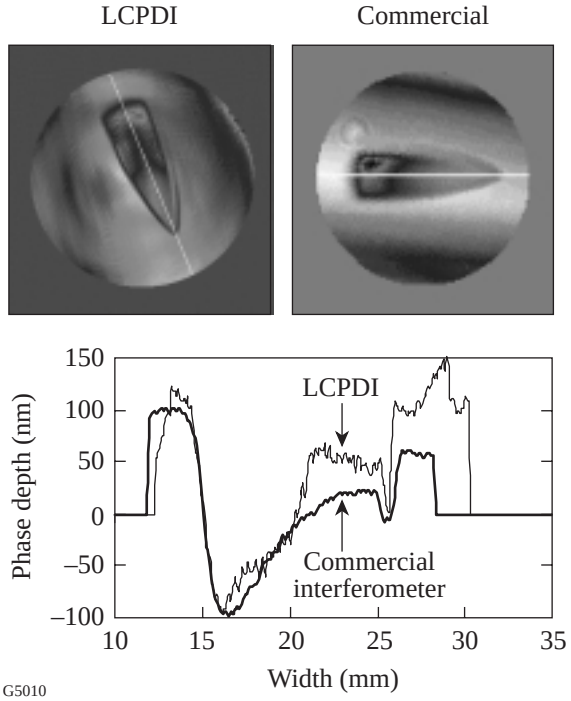

Figure 83.34
Phase measurements of a wedged window containing an MRF polishing spot comparing the LCPDI to a commercial interferometer (Zygo Mark IV XP). The LCPDI lineout matches that of the Zygo Mark IV in some areas and is ≤50 nm discrepant in other areas primarily due to the absorption dichroism of the dye used.

intensity remains constant with applied voltage and (2) the object beam intensity can be accurately measured. Although the object beam intensity is fairly well approximated using the procedure described above, a ray-trace model has shown that the intensity of the reference beam changes with voltage applied to the cell.[16,17] This model has also indicated that refraction through the microsphere cannot produce sufficient intensity in the reference beam to obtain the experimentally observed high fringe contrast, and diffraction must also be considered.[17] This suggests that by measuring fringe contrast and object-beam-intensity changes with voltage, it may be possible to accurately account for changes in reference beam intensity and thereby further reduce the phase error contributed by the absorption dichroism of the dye. Nonetheless, frame-to-frame absorbance changes in the LCPDI can be substantially reduced through the use of either a non-dichroic dye or a mixture of both positive and negative dichroic dyes. In Fig. 83.35, the absorbance as a function of wavelength for two such positive and negative dichroic dye combinations in E7 is shown for different voltages applied to the cell.[18] Figure 83.35(a) shows that when the Oil Red O dye, having positive dichroism, was combined with a negative dichroic Orasol dye mixture, the OD at 543 nm in a 22-μm-path cell changed by only 0.03 as the voltage was increased from 0 to 5-V rms. This result represents a factor-of-40 improvement compared with absorbance changes observed in the cell with the single dye component Oil Red O (compare with Fig. 83.31). An Orasol/Sudan dye mixture in Fig. 83.35(b) showed a change in OD of only 0.08 as voltage changed by 9-V rms. These results are summarized in Table 83.IV. We are currently in the process of purifying the Orasol dyes in order to reduce ionic conduction in the LC that has contributed to hydrodynamic-induced scattering observed in devices made with the new dye mixtures. Because the molecular structure of the Orasol dyes is not well known, the effect of these dyes on the long-range orientational order of the LC is currently unknown. Other visible-wavelength dye candidates with negative absorption dichroism that are expected to minimally perturb the liquid crystalline order parameter have also recently been identified.[19] For applications at λ = 1054 nm, LCPDI's fabricated using recently synthesized nickel dithiolene dyes with various terminal functional groups[20] also show significantly less intensity change as a function of voltage applied to the cell. It is anticipated that appropriate combinations of purified positive and negative dichroic dyes will substantially reduce, or even eliminate, the primary source of systematic error in the LCPDI.

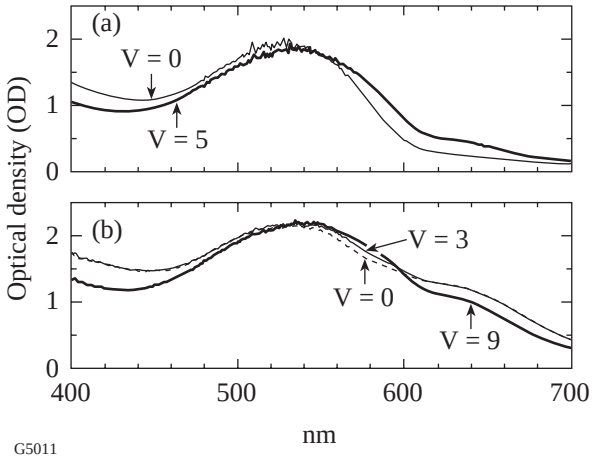

Figure 83.35
Absorbance (OD) of two different dye mixtures containing both positive and negative dichroic dye components in E7 shows very little change with applied voltage. Such mixtures can be used to significantly reduce phase-shift error in the LCPDI caused by the absorption dichroism of a single dye. (a) 1.3% Orasol Red BL, 0.55% Orasol Black RLI, + Oil Red O; (b) 1.3% Orasol Red BL, 0.55% Orasol Black RLI + 0.2% Sudan III, 0.38% Sudan Black B. In each case fluid path length was 22 μm.

2. LC Host-Induced Measurement Error

Although the long-range orientational order of the LC is homogeneous and planar, we have observed a distortion in the molecular alignment locally around the microsphere that is voltage dependent and can lead to phase-shift errors.[11] This alignment distortion is caused by a competition between anchoring forces on the surface of the sphere, the cell walls, and elastic forces of the LC.[21] Viewed through a polarizing microscope with 100× magnification, the liquid crystal alignment around the microsphere has the appearance shown in Fig. 83.36. These images are of a 10-μm-diam silica micro-

Table 83.IV: Absorbance (OD) at 543 nm.

V (rms at 2 kHz)	Mixture A	Mixture B
0	1.854	2.13
1	–	–
3	–	2.2
5	1.823	–
9	–	2.21
A = 1.3% Orasol Red BL, 0.55% Orasol Black RLI, + ORO		
B = 1.3% Orasol Red BL, 0.55% Orasol Black RLI + 0.2% Sudan III, 0.38% Sudan Black B		

sphere within the 10-μm path cell of E7 with 1% wt/wt Oil Red O dye used for the comparison tests described in the previous section. The alignment perturbation has quadrupolar symmetry, most apparent at intermediate rms voltages (2.38 V and 3.9 V in Fig. 83.36). The buff direction of the cell can be seen as oriented diagonally from the lower left to the upper right of these images. Regions of director distortion that have the appearance of large "ears" and extend outward from the sphere in the buff direction can also be seen in these images. This alignment distortion is enhanced in a thicker, 20-μm path cell with 20-μm-diam glass microspheres, shown in Fig. 83.37. In the thicker cell, the planar anchoring force of the substrate walls has less effect in the bulk of the fluid, and the alignment perturbation at intermediate voltages is more pronounced than in the 10-μm path cell. The director distortion appearing as large ears in these images again extends parallel to the buff direction. In Figs. 83.36 and 83.37, the increased electric-field strength encountered at higher voltages imparts sufficient torque to the molecules to overcome the competing surface-anchoring forces and elastic distortions of the liquid crystal, and the perturbation becomes less severe.

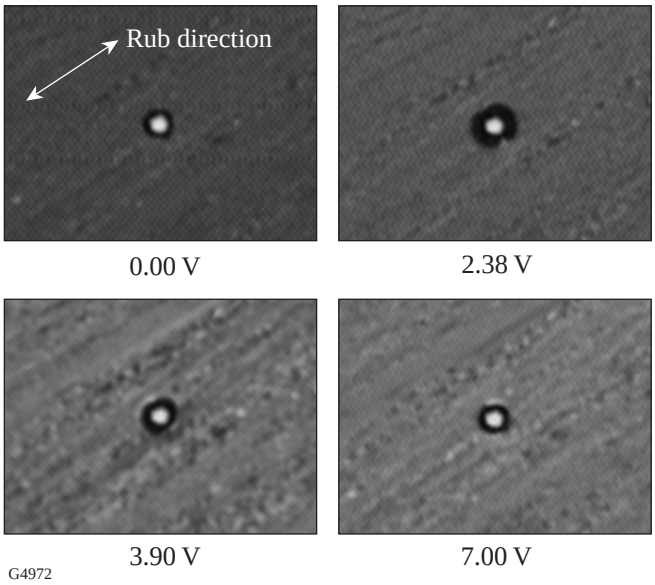

Figure 83.36
Polarizing microscope images of a 10-μm silica microsphere in 10-μm-path E7 host showing the quadrupolar alignment perturbation of the nematic director around the microsphere. This alignment perturbation produces a phase-shift error in the LCPDI that is dependent upon focusing conditions and the voltage applied to the cell. The quadrupolar symmetry is greatest at intermediate voltages, gradually becoming more circular with increasing electric-field strength. Voltage waveform was a 2-kHz sine wave.

The structures observed in Figs. 83.36 and 83.37 are similar to those described by other authors in the context of colloidal suspensions in nematic solvents[22,23] and inverted nematic emulsions.[21,24] The existence of planar or normal anchoring of the director to the sphere's surface plays a critical role in determining the director field configuration around the sphere[21] as does the anchoring strength.[25] For strong anchoring conditions, topological defects are known to form at the sphere's surface in addition to director distortions in the region surrounding the sphere.[21] With no voltage applied to the cell in Fig. 83.37, two such surface defects can be seen at the poles of the spheres that are diametrically opposed in a direction orthogonal to the long-range orientational order imposed by the substrates. We observed that altering the procedure by which the microspheres were applied to the surface of the substrates changed the topological orientation of the defects. In the images of Figs. 83.36 and 83.37, spheres were spin-deposited in a high-performance liquid chromatography-grade hexane solution onto one of the substrates, and the hexane was allowed to evaporate before the cells were filled with liquid crystal *via* capillary action. The alignment of the defects orthogonal to the rub direction of the substrates and the concomitant quadrupolar symmetry around the microsphere resemble structures characteristic of weak normal anchoring.[25] When a manual deposition method was used without hexane, however, the two surface defects appeared *along* the rub direction, providing evidence of planar anchoring at the surface of the sphere.[21] The change in anchoring conditions is

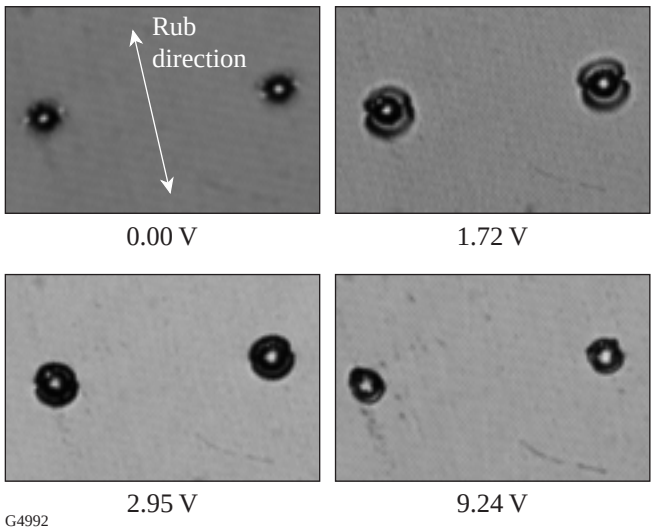

Figure 83.37
Polarizing microscope images of a 20-μm silica microsphere in 20-μm-path E7 host. The alignment distortion is enhanced, compared with the thinner LC cell of Fig. 83.36. Voltage waveform was the same as in Fig. 83.36

likely related to trace impurities that remained on the surface of the sphere after solvent evaporation since no attempt was made to further purify the hexane prior to use.

The effect of the quadrupolar alignment around the microsphere on a laser beam, when focussed close to the sphere, is clearly seen in Fig. 83.38. These interference fringes were obtained by using the setup shown in Fig. 83.32, and the small diffraction rings in Fig. 83.38 are from the final telephoto imaging lens. No measurable amount of light was observed to couple into the orthogonal polarization due to localized director distortions. Because the dye molecules rotate with the liquid crystal molecules, the dichroism of the Oil Red O dye in this cell may also have a contributing effect on the intensity and contrast changes observed. Focusing at a greater distance from the sphere produced fringes where the quadrupolar symmetry was less evident, as shown in Fig. 83.39. The loss of contrast caused by lower dye absorption of the object beam intensity can be clearly seen at 7.17 V in Fig. 83.39. As in Figs. 83.36 and 83.37, the effect of director distortions on the fringes in Figs. 83.38 and 83.39 is greatest at intermediate voltages. As the size of the Airy disk becomes increasingly larger compared with the size of the diffracting region, the reference wavefront becomes increasingly spherical,[8] with the optimum focusing condition for this device shown in Fig. 83.33(a).

These director distortions produce a phase-shift error that is both spatially nonuniform and nonlinear and can contribute significant residual phase error when the focus is placed very close to the microsphere. We have investigated the use of phase-shift algorithms designed for nonlinear and spatially nonuniform phase shifts, such as described by Hibino *et al.*,[26] to reduce these errors in the LCPDI. As described below, a six-frame algorithm designed to reduce the contribution of higher-order nonlinearity in the phase shift generally did not experimentally produce lower residual phase error than the five-frame algorithm produced. To explore the cause of this result, we have empirically derived a general form of the LCPDI phase-shift error with which we have compared the ability of each algorithm to reduce the contribution of director distortions to the phase measurement. A comparison of the residual phase error produced using these two algorithms in the absence of absorption dichroism was performed by subtracting a reference phase image created using error-free simulated fringes from the simulated phase image generated using the empirically derived phase-shift error.

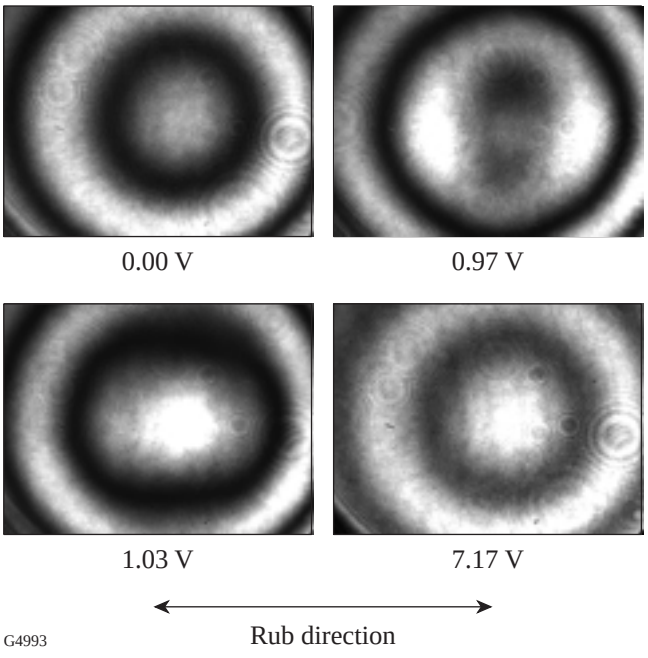

Figure 83.38
Interference fringes obtained by focusing a 543-nm laser beam at *f*/16 into the LCPDI of Fig. 83.36, revealing the effect of director distortions having quadrupolar symmetry.

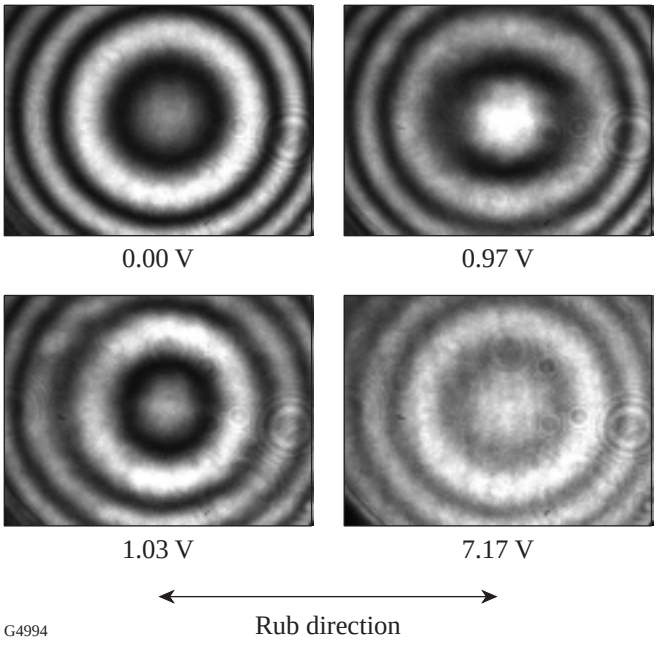

Figure 83.39
Interference fringes as in Fig. 83.38, but with displaced focal position. Quadrupolar symmetry is less evident at intermediate voltages than in Fig. 83.38. Loss of contrast due to dichroism of the Oil Red O dye molecules is observed at high voltage.

Neglecting frame-to-frame intensity and contrast changes, the intensity $I(x,y,\alpha_r)$ of each frame of data can be written as

$$I(x,y,\alpha_r) = I_0(x,y)\{1+\gamma(x,y)\cos[\alpha_r - \phi(x,y)]\}$$

$$\text{for } r = 1, 2, \ldots, m, \tag{2}$$

where $I_0(x,y)$ is the mean intensity, γ is the interference fringe visibility, α_r is the phase shift at each discrete frame r, ϕ is the phase of the wavefront being measured, and m is the total number of frames. Here the phase-shift parameter α_r is spatially nonuniform and changes nonlinearly from frame to frame. Following Ref. 26, α_r can be given by a polynomial expansion of the unperturbed phase-shift value α_{0r} as

$$\alpha_r = \alpha_{0r}[1+\varepsilon(\alpha_{0r})]$$

$$= \alpha_{0r}\left[1+\varepsilon_1(x,y)+\varepsilon_2(x,y)\frac{\alpha_{0r}}{\pi}+\varepsilon_3(x,y)\left(\frac{\alpha_{0r}}{\pi}\right)^2\right.$$

$$\left.+\ldots+\varepsilon_p(x,y)\left(\frac{\alpha_{0r}}{\pi}\right)^{p-1}\right]$$

$$\text{for } r = 1, 2, \ldots m, \tag{3}$$

where p ($p \le m-1$) is the maximum order of the nonlinearity, ε_q ($1 \le q \le p$) are the error coefficients, which can be spatially nonuniform, and $\alpha_{0r} = 2\pi[r-(m+1)/2]/n$ is the unperturbed phase shift with n equal to an integer. For the five-frame algorithm in Eq. (1), for example, $m = 5$, $n = 4$, and the unperturbed phase shifts are therefore

$$\begin{aligned}
\alpha_{01} &= -\pi, \\
\alpha_{02} &= -\pi/2, \\
\alpha_{03} &= 0, \\
\alpha_{04} &= \pi/2, \\
\alpha_{05} &= \pi.
\end{aligned} \tag{4}$$

The offset value $(m + 1)/2$ was introduced in Ref. 26 for convenience of notation and adds only a spatially uniform piston term to the calculated phase when no phase-shift error is introduced. In the simulation that follows, the functional form of the phase-shift error and the starting phase value were chosen to closely represent the experimentally observed phase-shift error. Equation (1) can correct for linear phase-shifter miscalibration (i.e., $p = 1$) that is spatially nonuniform but is sensitive to the effect of spatial nonuniformity for higher orders of phase-shift error.[26] The six-frame algorithm [Eq. (39)][26] given by

$$\tan\phi = \frac{\sqrt{3}(5I_1 - 6I_2 - 17I_3 + 17I_4 + 6I_5 - 5I_6)}{I_1 - 26I_2 + 25I_3 + 25I_4 - 26I_5 + I_6} \tag{5}$$

has greater immunity to both linear and quadratic nonlinearity ($p = 2$) of the phase shift that is spatially nonuniform. For this algorithm, the phase-shift interval is $\pi/3$, and $m = n = 6$. For both the five- and six-frame algorithms given by Eqs. (1) and (5), respectively, the phase ϕ was calculated using fringes simulated with Eq. (2), where the object beam intensity in Eq. (1) was taken as constant from frame to frame. As noted previously, a comparison of the residual phase error from these two algorithms was performed by subtracting a reference phase image ϕ_{ideal}, created by using error-free simulated fringes, from the phase image $\phi_{\text{perturbed}}$, generated using the empirically derived phase-shift-error coefficient

$$\varepsilon(\alpha_{0r}) = H\exp[-A\alpha_{0r}] \times f(x,y), \tag{6a}$$

where α_{0r} is the unperturbed phase shift and the spatial nonuniformity is given as

$$f(x,y) = \left[1-\exp\left(-\left|Bx^2+Cy^2\right|\right)\right]$$

$$\left\{\exp\left[-\left|\left(Dx^2+Ey^2\right)^{1/2}/F\right|^G\right]\right\}$$

$$\times\left|\sin\left[\tan^{-1}(Kx/My)\right]\right|, \tag{6b}$$

where A–M are constants. The phase shift used in generating $\phi_{\text{perturbed}}$ was calculated by combining Eqs. (6) and (3):

$$\alpha_r = \alpha_{0r}[1+H\exp(-A\alpha_{0r})\times f(x,y)]. \tag{7}$$

Figure 83.40 shows the general form of $f(x,y)$ and the peak value of the phase error in Eq. (7) as a function of α_{0r} for one set of constants A–M with $A > 0$. The functional form of this phase error is qualitatively similar to the director distortion observed in Figs. 83.36 and 83.37; the interference fringes in

Fig. 83.41, simulated using Eqs. (2) and (7) and used to obtain $\phi_{\text{perturbed}}$, are similar in appearance to those in Figs. 83.38 and 83.39. It is likely that some of the experimentally observed spatial variations in fringe intensity and contrast when focused close to the microsphere can be attributed to spatially nonuniform absorbance caused by orientational coupling between the dye molecules and liquid crystal molecules. We have not attempted here to model dye-induced absorbance changes that may affect fringe intensity and contrast. The image containing the residual phase error is thus given as

$$\Delta\phi = \phi_{\text{perturbed}} - \phi_{\text{ideal}}. \tag{8}$$

By expanding the exponential term in Eq. (7) and comparing with Eq. (3), it can be shown that the linear and quadratic error terms are, respectively,

$$\varepsilon_1 = H f(x,y), \qquad \varepsilon_2 = -AH\pi f(x,y), \tag{9}$$

and Eq. (7) can be approximated by

$$\alpha_r = \alpha_{0r}\left[1+\varepsilon(\alpha_{0r})\right] \approx \alpha_{0r}\left[1+\varepsilon_1(x,y)+\varepsilon_2(x,y)\frac{\alpha_{0r}}{\pi}\right] \quad \text{for } r = 1,\ 2,\ \ldots, m, \tag{10}$$

where $\varepsilon_1(x,y)$ and $\varepsilon_2(x,y)$ are given by Eq. (9). The ability of this approach to determine which algorithm would experimentally show better immunity to LCPDI phase-shift errors in the absence of absorption dichroism was first tested theoretically using Eq. (10) with spatially uniform error coefficients ε_1 and ε_2 [i.e., $f(x,y) = 1$]. Table 83.V compares these results with the results of Hibino *et al.*[26] The residual errors shown in this table for the six-frame algorithm matched those of Ref. 26, and this algorithm performed significantly better than the five-frame algorithm when the quadratic phase-shift error shown in the table was introduced. The six-frame algorithm also produced less residual phase error when the spatially nonuniform error term given by Eq. (6b) was included in the simulated phase plots. When the phase error was exponentially increasing (i.e., ε_1, $\varepsilon_2 > 0$), the six-frame algorithm consistently yielded less residual error than the five-frame algorithm. When $\varepsilon_2 < 0$, however, the five-frame algorithm generally yielded less residual error. Table 83.VI gives a relative comparison of the algorithms using spatially nonuniform ε_1 and ε_2 given by Eq. (9) for both positive and negative values of ε_2. For the cases when $\varepsilon_2 < 0$, the sum of the phase-shift error terms in Eq. (10) yields an approximation to the shape of the curve shown in Fig. 83.40; the descriptive terms in Table 83.VI when $\varepsilon_2 < 0$ correspond to the different regions of this curve. Among the curve shapes listed in Table 83.VI, the "parabola" most closely approximates the observed LCPDI phase-shift error, and the five-frame algorithm gave less residual phase error in this case.

Residual phase errors from both algorithms using experimental fringes are compared in Table 83.VII with residual phase errors obtained using fringes simulated with the phase perturbation given by Eq. (7) and shown in Fig. 83.40. To avoid unwrapping errors observed when excessive phase error is introduced, an intermediate focusing regime that showed sufficient host-induced phase error was chosen for this test. Figure 83.42(a) compares two experimental interferograms from this series with their corresponding simulated interferograms. As shown in Table 83.VII, the five-frame algorithm produced lower residual rms phase error in both the experiment and the simulation by nearly the same factor. The larger p–v errors in

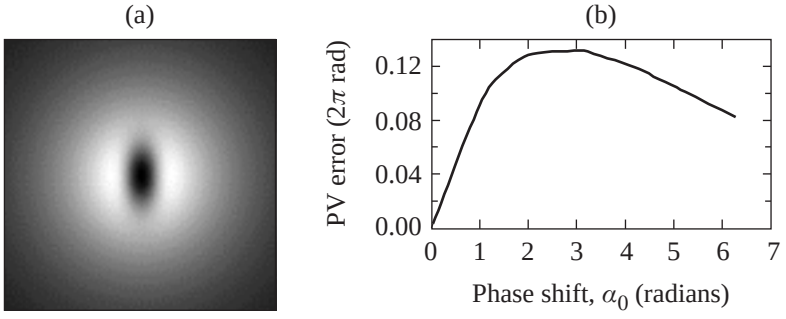

Figure 83.40
(a) Gray-scale image showing the spatial form of $f(x,y)$ defined in the text and used in Fig. 83.42. Black corresponds to $f(x,y) = 0$ with a maximum value of $f(x,y) = 1$. (b) Peak value of the phase-error function $\alpha_{0r}[\exp(-A\alpha_{0r})\ f(x,y)]$ versus α_{0r} for the set of constants A–M given in Table 83.VII.

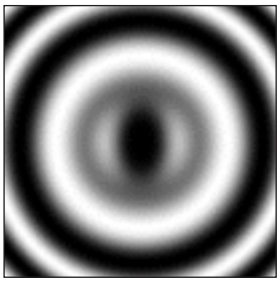

G5013

Figure 83.41
Simulated interference fringes computed using the empirically derived form of the LC alignment perturbation given by Eq. (7) and the two-beam interference expression given by Eq. (2). The simulated fringes are similar in appearance to the experimental fringes in Figs. 83.38 and 83.39.

the experimental results are attributed to spurious phase spikes. The ideal phase image ϕ_{ideal} in the experimental data set was determined from a five-term Zernike fit to the final phase image $\phi_{perturbed}$; the phase difference $\Delta\phi = \phi_{perturbed} - \phi_{ideal}$ is shown in Fig. 83.42(b). To reduce the contribution of dye-induced absorbance changes, each intensity interferogram in the experimental data set was normalized by a reference intensity image obtained adjacent to the microsphere at the same voltage. In both the experimental and simulated fringes, the phase perturbation was observed to first increase, then decrease in amplitude as the phase was shifted through the requisite number of frames, corresponding to $A = 0.37$ and $H = 1.21$ in Eq. (7). For the experiment, the starting phase corresponded to a voltage close to the Frederiks transition threshold where very little perturbation in the fringes was

Table 83.V: Peak-to-valley residual phase errors (2π rad) that are due to linear and quadratic spatially uniform phase-shift errors for the five- and six-frame algorithms.

ε_1	ε_2	Five-Frame	Six-Frame	Six-Frame*
0.1	0.0	0.0020	0.00005	0.00005
0.0	0.2	0.0265	0.0015	0.0015
0.1	0.2	0.0260	0.0025	0.0025
0.0	0.4	0.0610	0.0060	0.0060
0.1	0.4	0.0595	0.0050	0.0050

*From Table 3 of Ref. 26.

Table 83.VI: Residual phase error (2π rad) produced by the five- and six-frame algorithms for different values of the quadratic error coefficient ε_2. The error coefficients were multiplied by the spatial nonuniformity $f(x,y)$ in each case before computing residual error using the values of constants B–M indicated. The descriptive terms refer to the shape of the curve produced by plotting the induced phase error given in Eq. (10) versus the phase shift α_{0r}.

ε_1	ε_2	Type		Five-Frame	Six-Frame
0.0833	–0.0139	Decreasing positive slope	rms	0.00490	0.00464
			p–v	0.03250	0.03010
0.0833	–0.0417	Parabola	rms	0.00236	0.00313
			p–v	0.01510	0.02030
0.0833	0.4629	Increasing exponential	rms	0.0601	0.0280
			p–v	0.2390	0.1780
0.0833	0	Linear	rms	0.00642	0.00533
			p–v	0.04100	0.03470
$B = 0.03$; $C = 0.008$; $D = E = 0.002$; $F = 2$; $G = 3$; $M = 0$.					

observed. Thus, in the simulation, a starting phase of $\alpha_{0r} = 0$ was used. The superior performance of the five-frame algorithm by nearly the same factor in both the simulation and the experiment suggests that the form of the LCPDI phase-shift error represented empirically by Eq. (7) may be the underlying cause of the experimentally observed discrepancy.

Generally, an algorithm with more sample frames will be more effective in reducing measurement errors, depending upon the type of phase-shift error addressed by the algorithm and the type of error introduced during the measurement. Currently a period of 2 to 3 s is required between frames to ensure that the liquid crystal molecules have reached an equilibrated state, thus choosing a phase-shifting algorithm that addresses LCPDI device-specific phase-shift errors and minimizes the number of frames required is critical. Multiple applications of the phase-offset method can also reduce higher-order phase-shift errors;[15] however, this method is limited by the maximum retardance that can be obtained in an LCPDI device. This simulation and the experimental results (1) confirm the superior performance of the five-frame algorithm over the six-frame algorithm for this LCPDI, even though the six-frame algorithm was designed to address higher-order phase-shift error, and (2) emphasize the importance of understanding the underlying behavior of the phase-shift error in the LCPDI in order to choose effective phase-reduction algorithms and to optimize experimental conditions. For example, further reduction of phase errors related to the liquid crystalline host

Table 83.VII: Comparison of residual errors (2π rad) obtained using the five- and six-frame algorithms with both experimental and simulated interference images. Simulated images were obtained using the indicated values of constants *A*–*M*, corresponding to the phase perturbation shown in Fig. 83.40.

	Experiment			Simulation	
	Five-Frame	Six-Frame		Five-Frame	Six-Frame
p–v	0.1450	0.278		0.1001	0.1314
rms	0.0167	0.022		0.0164	0.0223
$H = 1.21498$; $A = 0.37$; $B = 0.06$; $C = 0.016$; $D = E = 0.002$; $F = G = 1$; $M = 0$.					

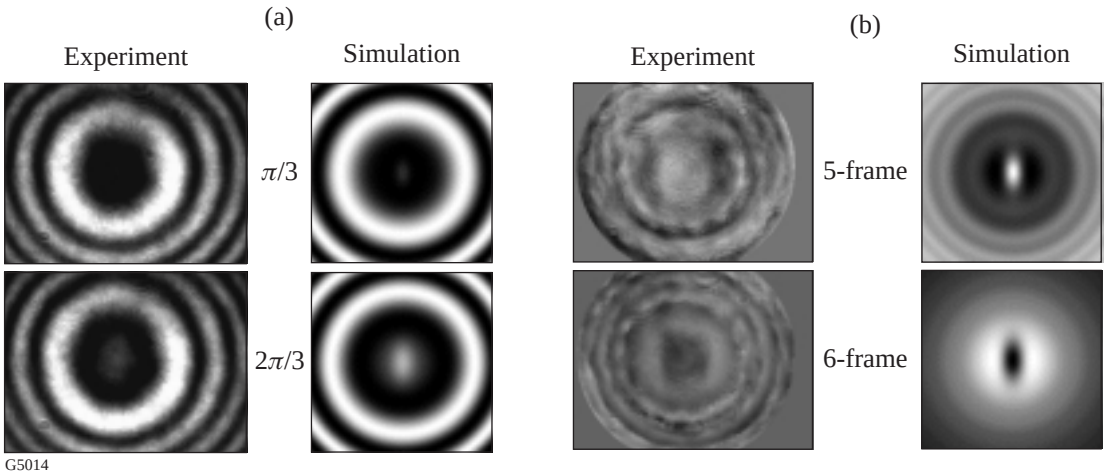

Figure 83.42
(a) Two interferograms from the six-frame series used in comparing five- and six-frame algorithms. For the images shown, the phase shift $\alpha_{0r} = \pi/3$ and $2\pi/3$, corresponding respectively to $r = 2, 3$ for the six-frame algorithm. Focusing conditions were chosen so as to introduce only a moderate amount of LC host-induced phase-shift error to avoid possible phase unwrapping errors. (b) Gray-scale images of the residual phase error $\Delta\phi = \phi_{\text{perturbed}} - \phi_{\text{ideal}}$ for the five- and six-frame algorithms. For the experimental results shown, ϕ_{ideal} was determined by a five-term Zernike fit to the phase data. Table 83.VII gives p–v and rms errors.

alignment distortions may be possible by tailoring an algorithm for the observed phase-shift error. In addition, operating the device well above the Frederiks transition threshold will reduce the alignment perturbation and thus also reduce the measurement error, once high-contrast fringes can be maintained in the higher-voltage regime through the use of a dye system without absorption dichroism. We have also begun to investigate the use of chiral-smectic-A LC's in place of nematic-phase LC's because of their faster response time, high birefringence, and gray-scale capability.[27,28] Liquid crystal systems with a faster response time would make algorithms with a greater number of sample frames more practical.

Summary

The liquid crystal point-diffraction interferometer is attractive in that it combines the common-path design of the PDI with the high resolution that can be achieved through modern phase-shifting techniques; it is also a low-cost alternative to commercially available phase-shifting interferometers. Empty-cavity measurements using the LCPDI designed for 543 nm with a dye having large absorption dichroism produced residual p–v and rms phase errors of 19 nm (0.035 λ) and 1.1 nm (0.002 λ), respectively, without using a phase-offset averaging technique and with nonideal environmental conditions. This suggests that LCPDI devices to be fabricated using newly available near-IR dyes[20] will satisfy the desired accuracy of 105 nm at λ = 1054 nm for *in-situ* analysis of OMEGA beamlines. Using the visible-wavelength LCPDI for phase measurement of a wedged window with a polished spot yielded results that were comparable to those of the Zygo Mark IV XP, showing the current LCPDI to be a useful optical metrology tool. The LCPDI measurement matched the Mark IV measurement nearly exactly in some regions but was ≤50 nm discrepant in other regions. This spatially dependent error had periodicity equal to that of the interference fringes, suggesting an intensity change from frame to frame caused by the absorption dichroism of the dye as the primary cause of the discrepancy. Additional error contributors in these measurements were interference effects of multiple beams and LC molecular alignment distortions around the mircrosphere.

The use of a non-dichroic dye or a combination of positive and negative dichroic dyes will significantly reduce errors related to intensity changes from frame to frame. For visible-wavelength applications, the high absorbance necessary to achieve high-contrast fringes has been available from commercially available dyes, whereas for applications in the near-IR, we have synthesized several dyes showing significantly greater absorbance than can be obtained from commercial dyes.[20] Two visible-wavelength dye mixtures that combine commercially available dyes having positive dichroism with Orasol dyes exhibiting negative dichroism were shown to have negligible change in absorbance over the voltage range of interest. Synthesis by-products not removed from the Orasol dyes may be the cause of the high ionic conduction measured in LCPDI cells made with these components, giving rise to a scattering texture that appeared when voltage was applied to the device. Purification of these dye components is in process, and it is expected that future LCPDI devices incorporating these purified dyes or other dye candidates will produce significantly less scatter. For wavefront analysis of OMEGA beamlines, initial tests of LCPDI devices fabricated using the newly synthesized near-IR dye mixtures show much less intensity change with voltage applied to the cell than that seen in the visible-wavelength devices, suggesting that some of these dye components may have negative dichroism.[20]

Our investigation has also shown that director distortions in the vicinity of the microsphere can affect phase-measurement accuracy of the LCPDI and suggests that it is possible to tailor device fabrication and experimental testing parameters to reduce the effect of nematic director distortions on phase measurements. Stronger anchoring in the bulk of the fluid, achieved by using a thinner path cell, was shown to reduce the spatial extent of the alignment distortion. Obtaining weaker anchoring at the sphere surface will likely reduce phase-measurement errors by eliminating topological defects and minimizing director distortions as voltage is applied to the cell.[25] These director distortions were observed to perturb the interference fringes when the focus was placed very close to the microsphere, although by judicious choice of focusing regime, the contribution of alignment distortions to the phase error was significantly reduced. Our simulation using the empirically derived phase-shift error suggests that phase-measurement error due to host alignment distortions can be further reduced through the use of device-specific phase-shifting algorithms, once these distortions become the dominant contribution to the measurement error.

It is expected that (1) the use of dyes that eliminate absorbance changes during data acquisition and (2) the reduction of acoustic vibration through the use of an air-supported table and more rigid mounting of the device will greatly improve LCPDI accuracy and precision, making the LCPDI a low-cost alternative for evaluation of high-performance optical elements, such as required for OMEGA. The use of phase-shifting algorithms and averaging methods tailored for device-specific phase-shift errors can further improve LCPDI performance.

ACKNOWLEDGMENT

This work was supported by the U.S. Department of Energy Office of Inertial Confinement Fusion under Cooperative Agreement No. DE-FC03-92SF19460, the University of Rochester, and the New York State Energy Research and Development Authority. The support of DOE does not constitute an endorsement by DOE of the views expressed in this article.

REFERENCES

1. K. Creath, in *Progress in Optics XXVI*, edited by E. Wolf (North-Holland, Amsterdam, 1988), Chap. V.
2. M. V. R. K. Murty, in *Optical Shop Testing*, edited by D. Malacara, Wiley Series in Pure and Applied Optics (Wiley, New York, 1978), Chap. 4, pp. 105–148.
3. V. P. Linnik, C.R. Acad. Sci. (USSR) **1**, 208 (1933).
4. R. N. Smartt and W. H. Steel, Jpn. J. Appl. Phys. **14**, 351 (1975).
5. D. Malacara, ed. *Optical Shop Testing*, Wiley Series in Pure and Applied Optics (Wiley, New York, 1978).
6. See, for example, several references in Ref. 8.
7. C. R. Mercer and K. Creath, Opt. Lett. **19**, 916 (1994).
8. C. R. Mercer and K. Creath, Appl. Opt. **35**, 1633 (1996).
9. C. R. Mercer and N. Rashidnia, in *8th International Symposium on Flow Visualization 1998*, edited by G. M. Carlomagno and I. Grant (Edinburgh, Scotland, 1998), CD-ROM, pp. 256.1–256.9.
10. Zygo Mark IVxp™, Zygo Corporation, Middlefield, CT 06455.
11. M. J. Guardalben and N. Jain, Opt. Lett. **25**, 1171 (2000).
12. J. Schwider *et al.*, Appl. Opt. **22**, 3421 (1983).
13. P. Hariharan, B. F. Oreb, and T. Eiju, Appl. Opt. **26**, 2504 (1987).
14. S. D. Jacobs, S. R. Arrasmith, I. A. Kozhinova, L. L. Gregg, A. B. Shorey, H. J. Romanofsky, D. Golini, W. I. Kordonski, P. Dumas, and S. Hogan, Am. Ceram. Soc. Bull. **78**, 42 (1999).
15. J. Schwider, T. Dresel, and B. Manzke, Appl. Opt. **38**, 655 (1999).
16. A. C. Turner, 1998 Summer Research Program for High School Juniors at the University of Rochester's Laboratory for Laser Energetics, Laboratory for Laser Energetics Report No. 300, NTIS document No. DOE/SF/19460-299 (1998). Copies may be obtained from the National Technical Information Service, Springfield, VA 22161.
17. R. Rao, 1999 Summer Research Program for High School Juniors at the University of Rochester's Laboratory for Laser Energetics, Laboratory for Laser Energetics Report No. 311, NTIS document No. DOE/SF/19460-338 (1999). Copies may be obtained from the National Technical Information Service, Springfield, VA 22161.
18. The Orasol dyes were recommended by C. Mercer, private communication.
19. E. Prudnikova, B. Umanskii, and T. Plyusnina, Mol. Cryst. Liq. Cryst. **332**, 37 (1999).
20. Laboratory for Laser Energetics LLE Review **81**, 37, NTIS document No. DOE/SF/19460-335 (1999). Copies may be obtained from the National Technical Information Service, Springfield, VA 22161.
21. P. Poulin and D. A. Weitz, Phys. Rev. E **57**, 626 (1998).
22. P. Poulin, N. Frances, and O. Mondain-Monval, Phys. Rev. E **59**, 4384 (1999).
23. A. Glushchenko *et al.*, Liq. Cryst. **23**, 241 (1997).
24. H. Stark, J. Stelzer, and R. Bernhard, Eur. Phys. J. B **10**, 515 (1999).
25. O. Mondain-Monval *et al.*, Eur. Phys. J. B **12**, 167 (1999).
26. K. Hibino *et al.*, J. Opt. Soc. Am. A **14**, 918 (1997).
27. S. Garoff and R. B. Meyer, Phys. Rev. A **19**, 338 (1979).
28. A. Sneh, J. Y. Liu, and K. M. Johnson, Opt. Lett. **19**, 305 (1994).